PROCEEDINGS OF SPIE

SPIEDigitalLibrary.org/conference-proceedings-of-spie

Aberrations in square pore micro-channel optics used for x-ray lobster eye telescopes

R. Willingale, J. F. Pearson, A. Martindale, C. H. Feldman, R. Fairbend, et al.

R. Willingale, J. F. Pearson, A. Martindale, C. H. Feldman, R. Fairbend, E. Schyns, S. Petit, J. P. Osborne, P. T. O'Brien, "Aberrations in square pore micro-channel optics used for x-ray lobster eye telescopes," Proc. SPIE 9905, Space Telescopes and Instrumentation 2016: Ultraviolet to Gamma Ray, 99051Y (18 July 2016); doi: 10.1117/12.2232946

SPIE.

Event: SPIE Astronomical Telescopes + Instrumentation, 2016, Edinburgh, United Kingdom

Aberrations in square pore micro-channel optics used for X-ray lobster eye telescopes

R. Willingale[a], J.F. Pearson[a], A. Martindale[a], C.H. Feldman[a], R. Fairbend[b], E. Schyns[b], S. Petit[b], J.P. Osborne[a], P.T. O'Brien[a]

[a]Department of Physics and Astronomy, University of Leicester, UK
[b]PHOTONIS France S.A.S., Avenue Roger Roncier, 19100 Brive, B.P. 520, 19106 Brive Cedex, France

ABSTRACT

We identify all the significant aberrations that limit the performance of square pore micro-channel plate optics (MPOs) used as an X-ray lobster eye. These include aberrations intrinsic to the geometry, intrinsic errors associated with the slumping process used to introduce a spherical form to the plates and imperfections associated with the plate manufacturing process. The aberrations are incorporated into a comprehensive software model of the X-ray response of the optics and the predicted imaging response is compared with the measured X-ray performance obtained from a breadboard lobster eye. The results reveal the manufacturing tolerances which limit the current performance of MPOs and enable us to identify particular intrinsic aberrations which will limit the ultimate performance we can expect from MPO-lobster eye telescopes.

Keywords: X-ray optics for astronomy

1. INTRODUCTION

The lobster eye geometry for X-ray imaging was first introduced by Angel (1979)[1] and the use of square pore micro-channel plates (MCPs) to realise the micro-channel plate optics (MPOs) in a lobster eye X-ray telescope was initially pursued by several authors.[2–5] The current generation of square pore MPO devices which can be used in this application are produced by PHOTONIS France SAS*. The geometry, illustrated in Fig. 1, comprises a square packed array of microscopic pores with a square cross-section arranged over a spherical surface with radius of curvature $R = 2F$ such that all the pores point towards a common centre of curvature. Reflections from the inside walls of the pores produce an image on a focal surface which is spherical with radius of curvature F. The size of each pore aperture is d and the axial length of the pores is L as indicated in Fig. 1. The L/d ratio of the pores determines the grazing reflection angles which contribute most to the effective collecting area of the optic. For X-ray applications the critical angle for grazing reflection is $\theta_c \approx E^{-1}\rho^{1/2}$ degrees where E is the photon energy in keV and ρ is the material density in gm/cm^3. To get the maximum effective area we require $\theta_c \approx (180/\pi)(2\sqrt{2}+1)d/L$ degrees so using a high density coating material like Iridium with $\rho = 22.65$ gm/cm^3 and working at a photon energy of ~ 1 keV the optimum L/d ratio is ~ 50. MPOs are manufactured with standard pore sizes of typically 20 or 40 μm so the plates thickness are in the range 1-2 mm. The point spread function produced by such an optic is shown in Fig. 2. Rays which suffer 2 grazing incidence reflections off adjacent sides of a pore (or an odd number of reflections in both the primary axes of the pore aperture) produce a spot focus. Rays which suffer 1 reflection (or an odd number of reflections in one aperture axis and even in the other) form the cross-arms and rays which suffer 0 reflections (or an even number in both axes) go straight through the plate and form a diffuse patch around the focused spot.

The size of the field of view depends only on the angular extent of the spherical optic and detector. In fact, if the optic and detector cover complete spheres the field of view is the entire sky. Providing the optic is quasi continuous, constructed from a tesselation of tiles with small gaps between for support, there is no vignetting and no change in the point spread function over the field of view. Lobster eye optics are therefore ideally suited

E-mail: zrw@le.ac.uk
*PHOTONIS France SAS, Avenue Roger Roncier, 19100 Brive La Gaillarde, France

Space Telescopes and Instrumentation 2016: Ultraviolet to Gamma Ray, edited by Jan-Willem A. den Herder, Tadayuki Takahashi, Marshall Bautz, Proc. of SPIE Vol. 9905, 99051Y
 · doi: 10.1117/12.2232946

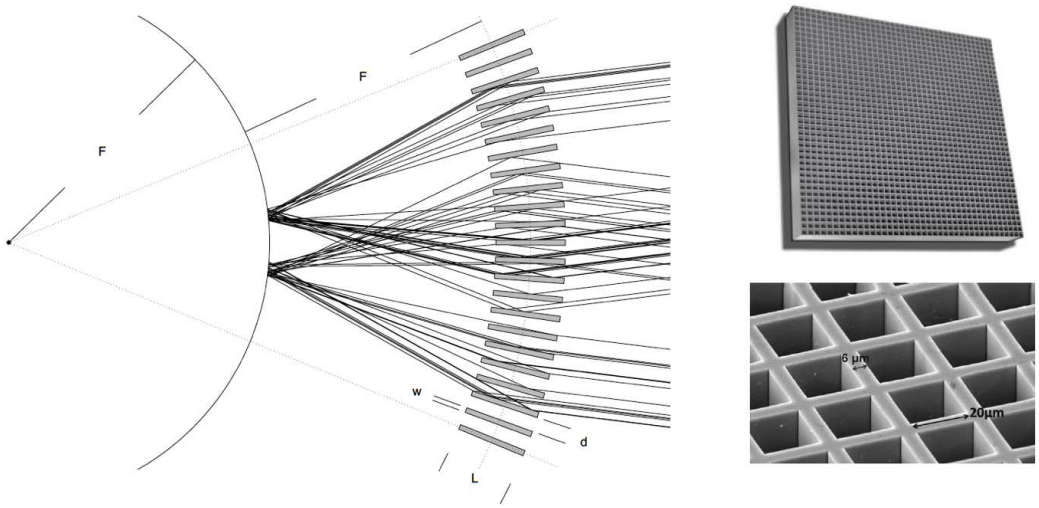

Figure 1. The lobster eye geometry. Top right: a schematic of a square pore MCP with simple square packing. Bottom right: a micrograph of the square pore apertures in a MPO. Left: Section through a ray tracing of a square packed array. Rays from two distant point sources are plotted. For clarity, those rays which pass directly through the pores without reflection or suffer > 1 reflection are not plotted.

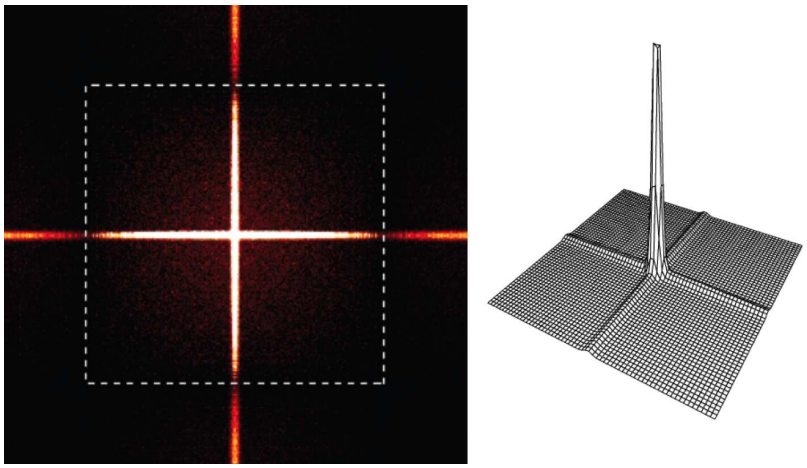

Figure 2. The cruciform point spread function. The dashed square indicates the off-axis angle position at which the cross-arm 1-reflection flux goes to zero, $\theta = 2d/L$. The projection to the right shows the central 2-reflection peak and the inner cross-arms.

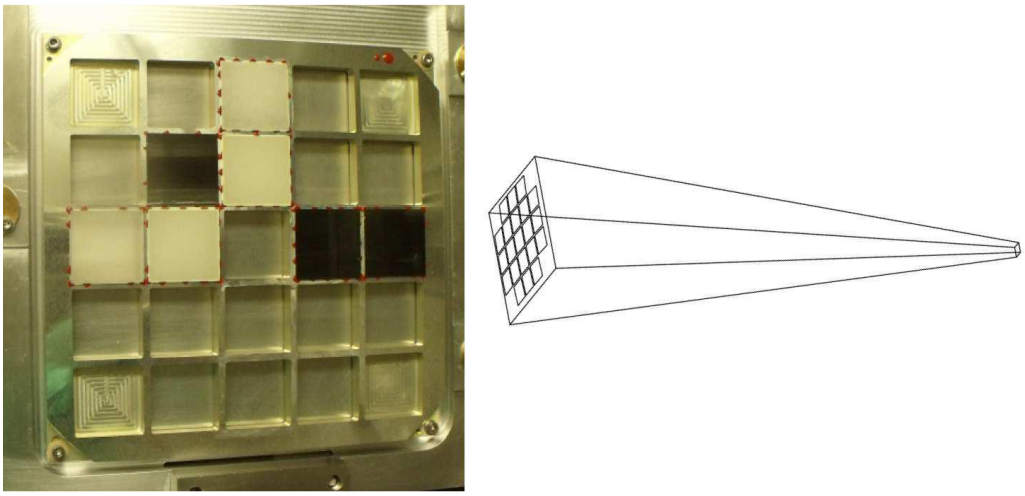

Figure 3. The breadboard optic with focal length $F = 1000$ mm. Right: a schematic of the optical bench. Left: the breadboard populated with 7 MPOs. 3 MPOs are coated with Iridium (the darker plates) and 4 are bare glass.

to very wide field applications or relatively narrow field instruments with very little vignetting. An example of a narrow field application is the *SVOM MXT*.[6]

We have constructed a breadboard of a narrow field optic as shown in Fig. 3. The optic comprises an array of 21 square pore MPOs each with an open aperture of 38 by 38 mm^2 and a radius of curvature of 2000 mm giving a focal length of 1000 mm. The field of view, defined by the off-axis angle at which the effective area from the optic at 1 keV drops to 50% of the on-axis value, is 6 degrees.

In this paper we address the intrinsic aberrations associated with the lobster eye geometry and imperfections in MPOs which limit the angular resolution and efficiency of lobster eye X-ray telescopes.

2. INTRINSIC ABERRATIONS

There are three instrinsic aberrations, associated with the lobster eye geometry, that limit the angular resolution performance independent of the technology used to construct the pore array. Spherical aberration gives an angular resolution of $\Delta\theta_s = 4\sqrt{2}(d/L)^3$, the geometric pore size limits the angular resolution to $\Delta\theta_g = d/F$ and diffraction limits the angular resolution to $\Delta\theta_d = 2\lambda/d$. Using the optimum $L/d = 50$ gives a spherical aberration limit of $\Delta\theta_s \approx 9$ arc seconds. In the absence of non-intrinsic aberrations the highest angular resolution will result if the pore size is chosen such that the geometric and diffraction limits are equal. We require $d = (2\lambda F)^{1/2}$ which yields $\Delta\theta_g = \Delta\theta_d = (2\lambda/F)^{1/2}$. If the photon energy is 1 keV and $F = 1$ m then $d = 50$ μm and $\Delta\theta_g = \Delta\theta_d \approx 10$ arc seconds. If we combine the spherical, geometric and diffraction limits, we get an intrinsic angular resolution at 1 keV of $(\Delta\theta_s^2 + \Delta\theta_g^2 + \Delta\theta_d^2)^{1/2} = \Delta\theta_i \approx 17$ arc seconds. Repeating this calculation for $F = 0.3$ m and using the same L/d gives an optimum pore size of $d = 27$ μm, $\Delta\theta_g = \Delta\theta_d \approx 19$ arc seconds, and an overall intrinsic angular resolution limit of $\Delta\theta_i = 28$ arc seconds.

The pore size, d, of available glass MCPs is well matched to the optimum angular resolution limits of the lobster eye geometry for X-ray telescope imaging in the energy band 0.1-10 keV. The MCPs can be produced with thicknesses, L, in the range 0.9-4 mm which gives the optimum $L/d \sim 50$ for efficient X-ray imaging in the same band. Using focal lengths larger than 1 m, more suitable for narrow field imaging instruments, the instrinsic angular resolution limit will be 10-20 arc seconds and for shorter focal lengths, more suited to wide field applications, the limit will be in the range 20-30 arc seconds.

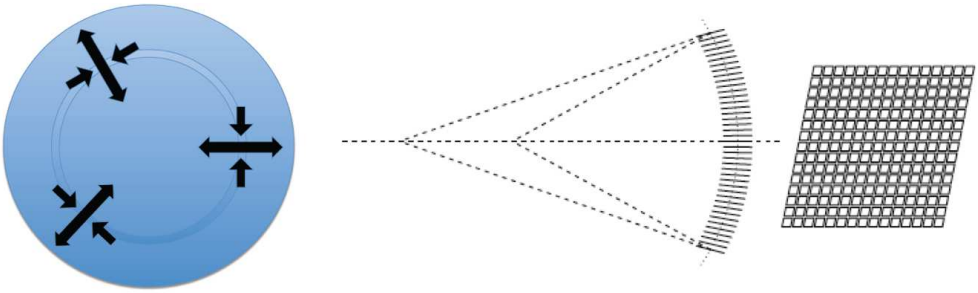

Figure 4. Intrinsic slumping errors. Left: azimuthal compression and radial expansion around each material annulus. Centre: the pores are tilted in the radial direction. Right: the square pore cross-section is distorted by shear.

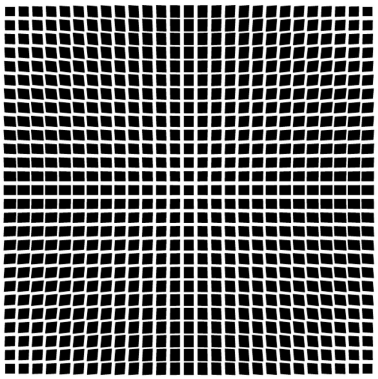

Figure 5. A schematic of the distribution of intrinsic pore shear errors expected from perfect slumping of a square plate.

3. INTRINSIC SLUMPING ERRORS

In the lobster eye geometry the pores must be arranged over a spherical surface and all the pores must point to a common centre of curvature. When using glass square pore MCPs this is achieved by *slumping* a flat plate into a spherical form using spherical mandrels and pressure at an elevated temperature. This process involves a necessary and intrinsic compression and stretching of the material as indicated in Fig. 4. Around each annulus of material we get azimithal compression and radial expansion which leads to pore radial tilt errors and pore cross-section shear errors as illustrated in Fig. 4. For a spherical slump radius of curvature R and a material annulus at radius r from the centre of the plate the tilt error is $\theta_a \approx r^2/(2R^2)$. This results in an angular shift in the focal plane of $\delta\theta_a = 2\theta_a = (r/R)^2$. The shear angle error (difference from 90 degree square corners in the pores) is $\theta_h \approx r\sin(2\theta)/R$, where θ is the azimuthal position of the pore on the plate. The angular shift in the focal plane introduced by this shear is $\delta\theta_h = \theta_h.\theta_g$ where θ_g is the grazing angle of reflection. The maximum contribution to focused flux in the focal plane comes from pores set at grazing angles $\theta_g \approx 2d/L$. Therefore the angular error due to pore shear is $\delta\theta_h \approx 2\sin(2\theta)(d/L)(r/R)$. If the plates are cut square with half width W_h before they are slumped then the compression/expansion distortions described here will relax in the corners and the tilt and shear errors will fall off for $r > W_h$. Fig. 5 shows the distribution of intrinsic slumping induced shear errors over a square plate. Pores close to the diagonals across the plate suffer the largest shear. Pores near the primary axes through the centre of the plate are free of shear errors although their square apertures become rectangular. We can estimate the contribution of the intrinsic slumping errors to the angular resolution by taking the average of $\delta\theta_a$ and $\delta\theta_h$ over the aperture of the square plate. Using an open aperture half width of $W_h = 19$ mm (which is typical using plates of full width 40 mm with a mounting loss of 1 mm around the edge of the plate) we get the mean tilt $\Delta\theta_a$ and mean shear $\Delta\theta_h$ angular resolution values listed in Table 1. The RSS of all the instrinsic components $\Delta\theta_t = (\Delta\theta_i^2 + \Delta\theta_a^2 + \Delta\theta_h^2)^{1/2}$ calculated for slumped square pore MCPs size 38×38 mm^2 and a pore $L/d = 50$ at an X-ray energy of 1 keV gives us an estimate of the angular resolution limit which would be obtained from perfect plates.

F mm	$\Delta\theta_i$	$\Delta\theta_a$	$\Delta\theta_h$	$\Delta\theta_t$
1000	0.28	0.17	0.60	0.68
300	0.47	1.88	1.99	2.78

Table 1. Angular resolution limits arc minutes: intrinsic aberrations $\Delta\theta_i$, intrinsic slumping tilt $\Delta\theta_h$, intrinsic slumping shear $\Delta\theta_h$. The final column $\Delta\theta_t$ is the RSS of the intrinsic components.

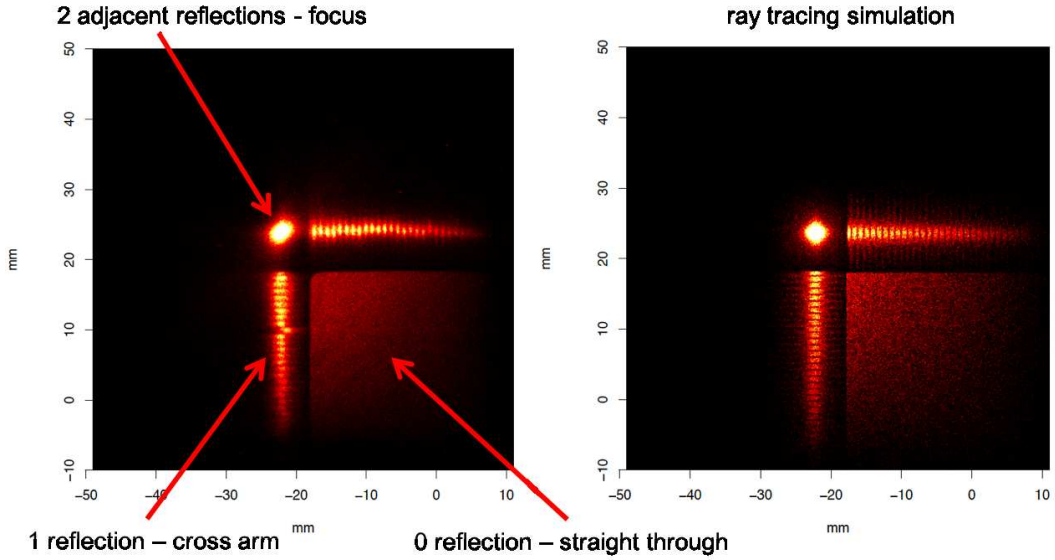

Figure 6. Left: X-ray image at 1.49 keV obtained from a single plate in the breadboard optic. Right: Simulation of the X-ray exposure created by ray tracing.

4. X-RAY MEASUREMENTS AND SIMULATION

Fig. 6 shows a typical X-ray image obtained from a single plate in the breadboard optic. The optic is tilted such that the source rays are normal to the spherical surface at a position a few millimeters away from the corner of the plate. The 2-reflection focused spot, the 1-reflection cross arms and the 0-reflection straight through patch are indicated. Such an exposure has obvious diagnostic power. The 3 primary components of the imaging response are separated on the focal plane and the image is self calibrating. The position of the focused spot with respect to the corner of the plate (pinpointed by the edges of straight through flux patch) tells us exactly where the source is in the frame of reference of the optic. The FWHM of the focused spot measured in images like Fig. 6 taken with the breadboard plates varies over the range 6.5-7.7 arc minutes depending on the plate and the corner of the plate used. One plate is obviously distorted and gives a FWHM of 9.8 arc minutes and this is discussed briefly later, in section 5.2.

The right-hand panel of Fig. 6 shows the ray tracing simulation of the observed image. The software model used includes all the aberrations discussed in this paper except for the diffraction by the pores. At a photon energy of 1 keV and pore size of 20 μm $\Delta\theta_d \approx 12$ arc seconds which corresponds to 0.06 mm in the focal plane, much smaller than the image pixel size, 0.15 mm, used in 6. The distortion and figure quality of every pore in the plate, the finite source position and position of the detector in the X-ray test facility are all included in the simulation.

The shadow of the corner of the plate marks the edge of the straight through patch. The diffuse flux fades as a function of radius from the focused spot towards the bottom right of the image. Fig. 7 shows the comparison of the measured and simulated surface brightness of this flux. The profile is determined by the L/d ratio and orientation of the pores and the spherical curvature of the plate. There is a close match between the data and simulation indicating that the plate geometry is simulated correctly. There are several distinctive features present in the observed data that are included in the simulation. The focused spot is not circularly symmetric but has a diamond or rectangular shape with the diagonal aligned to the cross arm axes (the primary axes of the pore packing in the plate). The cross arms are modulated by stripes and they are not completely straight.

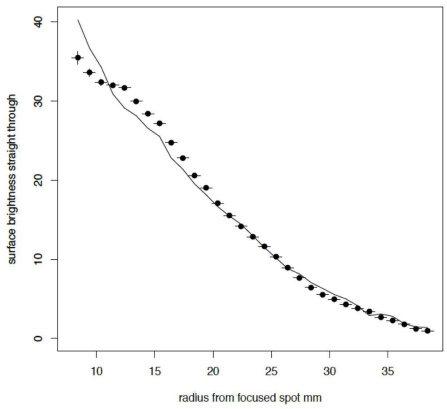

Figure 7. The surface brightness of the straight through patch as a function of radius from the focused spot. The solid line is the simulated data and the points are the X-ray measurements.

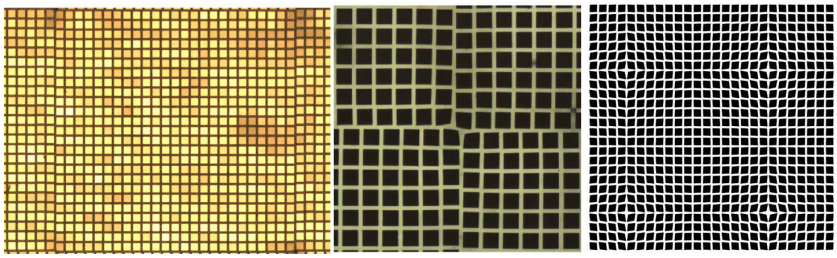

Figure 8. Left: optical micrograph of a 25 by 25 pore multifibre in a plate with $d = 40$ μm. Middle: a typical intersection between multifibres. Right: the model of the multifibre shear error distribution used in the ray tracing software. (The number of pores across the model multifibre has been reduced so that the shear error pattern is easier to see.)

Examination of these and other features in the X-ray images and comparison with the simulations has enabled us to identify the major aberration components in the MPOs and these are discussed below.

5. MANUFACTURING ERRORS

In addition to the instrinsic aberrations and slumping errors discussed above we must consider the imperfections which arise from the MCP manufacturing process.

5.1 Multifibre structure

The plates are manufactured from multifibres which are stacked and fused together. Each multifibre contains 35 by 35 pores in plates for which $d = 20$ μm and 25 by 25 pores when $d = 40$ μm and the packed arrays of multifibres are regular but not perfect. Pores near the intersection of 4 multifibres can be distorted and tilts or lateral displacements occur between adjacent rows or columns in the array as illustrated in Fig. 8. Lateral displacements of pores within the array have no effect on the optical response but shearing of the square pores and tilt errors do. Using the formulae above a shear angle of $\theta_h = 25$ arc minutes will give a focusing error $\Delta\theta_h \approx 1$ arc minute. We have modelled the shear errors associated with the multifibres using $\theta_h = A\exp(-r_f^2/2\sigma_f^2)$ where r_f is the radial distance of a pore from the intersection corners in the multifibre array and $\sigma_f \approx 4d$. This gives the distribution illustrated in the right-hand panel of Fig. 8. The amplitude is $A \approx 4$ degrees.

The very large shear angle errors which are visible near the multifibre intersection in Fig. 8 introduce major deflections of the X-ray flux. The affected pores remove flux from the focused spot and cross arms and push it out of the field of view. This is what causes the missing stripes in the cross arms visible in Fig. 6. The pitch of the stripe pattern exactly matches the periodicity of the multifibre packing, 0.855 mm for the plates under test.

Because of the way the plates are constructed, from an array of multifibres, tilt errors are introduced between rows and/or columns of multifibres. These tilt errors will necessarily be aligned to the principle axes of the

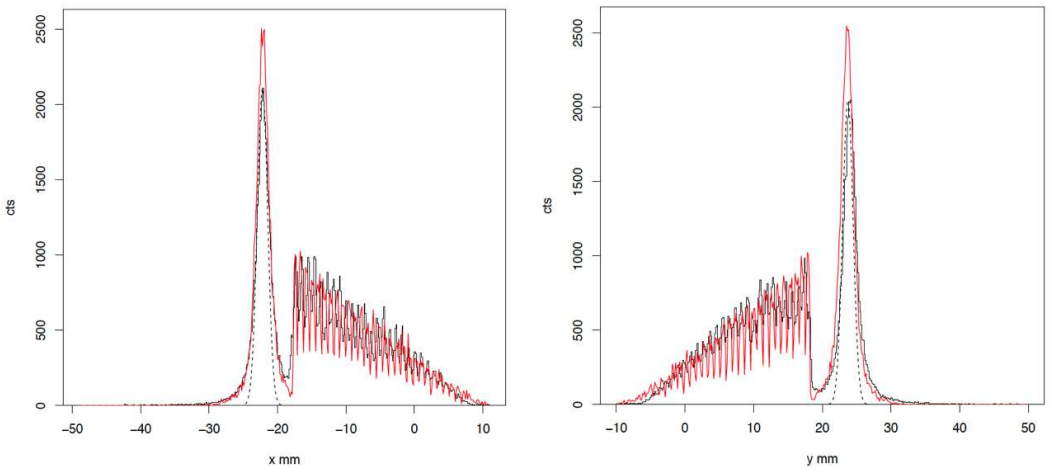

Figure 9. Profiles along the horizontal and vertical cross-arms extracted using a strip 1.05 mm wide. The histograms are the measured X-ray data and the continous red curves are the simulation. The dashed gaussian profiles have the same FWHM as the focused spot.

packing. They give rise to the diamond shape of the focused spot and introduce the displacements and waviness in the cross arms visible in Fig. 6. In the vertical cross arm there is one row of multifibres which is clearly tilted with respect to the bulk.

Fig. 9 shows the profiles along the horizontal and vertical cross arms extracted from the images in Fig. 6 using a strip 1.05 mm wide. The simulation is not a formal fit to the data. The parameters used in the model were chosen to give a reasonable match with the performance of the breadboard plates. The FWHM of the focused spot is 7.2 arc minutes. There was no attempt to match the phase of the multifibre packing observed to the multifibres with the simulation so the peaks and troughs of the striped pattern along the arms don't match although the period is correct and the amplitude is about right.

In addition to shear and tilt errors, for which the reflecting surfaces remain as flat planes, there are almost certainly pore wall figure errors associated with the multifibre structure although we can't observe or measure such errors in a simple way. The reflecting surfaces within each pore will be bent or twisted to some degree and a substantial fraction of the width of the cross arms and the size of the focused spot in the point spread function are attributable to such figure errors. The profile of the focused spot and cross arms appears to have two components. There is a central gaussian core and broader wings. The central core is indicated by the dashed profile plotted in Fig. 9 and the broad wings, which are present in both the data and the model, are clearly visible. In the simulation these are modelled by two distinct populations of pore. Those in the central regions of the multifibres which have low amplitude figure errors and those around the edges of the multifibres which suffer additional distortion during the manufacturing process and hence have larger figure errors. If we take the central core as 25 by 25 pores and the rest from a band of 5 pores wide around the edge then the split between the populations is approximately 50:50. The outer population has an rms figure error ~ 4 times greater than the inner population. Of course we could achieve the same effect if we used a continuous degradation in figure quality from the centre of the multifibres to the edge and in reality this is more likely to be the case.

5.2 Global errors

Some fraction of the pore tilt, shear and figure errors are not associated with the multifibre structure but come from processes which introduce errors globally across the MCPs. The plates are cut from a block and the pores may not be perpendicular to the surface as illustrated in Fig. 10. This so-called bias angle error has no effect on the performance of a single plate but presents a problem when we try to align several plates within a single aperture as is the case for the breadboard design, Fig. 3. A potentially much more serious problem is a variation in the bias angle of the pores across the surface of the MCP which may be introduced during the slumping process. This is a tilt error that varies in some systematic way across the plate and it will introduce bends or

Figure 10. Bias angle errors. Left: the pore should be perpendicular to the surface. Right: cutting tolerances can produce a bias angle error.

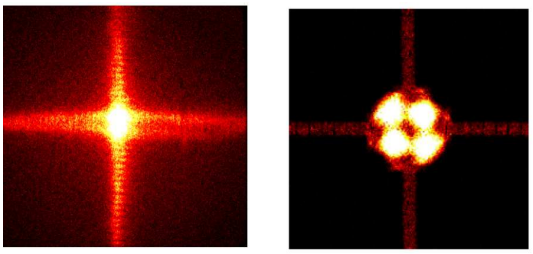

Figure 11. Left: Image obtained from a plate in which the bias angle varies across the plate. Right: a simulated image of the focused spot produced using a plate with a global shear error.

splits in the cross arm images and a serious blurring of the focused spot. This is the case for the plate used to produce the image in Fig. 11. The horizontal cross arm and the central focus are split into two and the FWHM of the focus is ~ 9.8 arc minutes. The manufacturing process can also introduce a global shear error so that the pore array looks like the distribution shown to the right in Fig. 4. The focus spot image produced is split into four lobes as shown by the simulated image in the right-hand panel of Fig. 11.

The etching process using to create the pores can generate axial figure errors over short length scales 50-500 μm and surface roughness on the reflecting surfaces. Brunton et al.[7] showed that, with the right processing, the surface roughness of channel walls of an MCP was 11 $\mathring{A}$ rms. Surface roughness measurements have not been carried out on the plates used in the present breadboard because the only reliable method involves breaking the plates and examining the channel walls. For the purposes of modelling we have assumed an rms roughness of 11 $\mathring{A}$ and a break frequency in the power spectrum of $\omega_b = 10$ mm^{-1}.

6. ANGULAR RESOLUTION

The best plate in the breadboard optic has a FWHM of 6.5 arc minutes. This is predicted by the simulation when we include the factors in Table 2. The radius of curvature of the plates is $R = 2000$ mm giving a focal length of $F = 1000$ mm. The position of the focal plane (and hence the effective focal length) is reduced by 38 mm when testing in the X-ray beamline which gives a source distance of 27 m. The large shear errors close to

	arc mins
geometric pore size $d = 20$ μm	0.07
spherical aberration pore $L/d = 50$	0.15
slumping - intrinsic radial tilt errors	0.17
slumping - intrinsic shear errors	0.60
surface roughness 11 $\mathring{A}$ rms, $\omega_b = 10$ mm^{-1}	2.46
figure errors at centre of multifibres	2.48
shear errors at centre of multifibres	-
multifibre tilt errors along primary axes	3.54
figure errors at edge of multifibres	9.92
shear errors at edge of multifibres	-
global shear errors	-
global tilt errors	-

Table 2. Contributions to the angular resolution that combine to give the best measured performance from a breadboard plate of 6.5 arc minutes FWHM.

the intersections between the multifibres introduce the stripe losses in the cross arms but don't contribute to the angular resolution budget. The figure error terms in Table 2 may include contributions from shear and global tilt errors. We are currently unable to distinguish between these contributions from the data and hence lump them together in cover-all figure error terms.

7. CONCLUSIONS

All the primary factors that introduce aberrations in the imaging performance of lobster eye optics have been identified. We have compared X-ray measurements of the performance of a breadboard lobster eye optic, constructed from MCPs manufactured by PHOTONIS France SAS, with a detailed software simulation in an attempt to identify and quantify the terms which dominate and limit the angular resolution. The intrinsic terms including the distortions inherent in the slumping process impose an ultimate limit in the range 1-3 arc minutes depending on the focal length. The MCPs in the breadboard optic have an angular resolution in the range 6.5-7.7 arc minutes. This performance is limited by the pore tilt errors, pore shear errors, and surface figure errors in the pores. These errors are introduced by a combination of faults in the multifibre structure within the plates and the slumping used to produce the spherical curvature. We are currently running further tests to try and understand which stages of the manufacturing chain are responsible for introducing the tilt and figure errors.

REFERENCES

[1] Angel, J. R. P., "Lobster eyes as X-ray telescopes," *ApJ* **233**, 364–373 (Oct. 1979).

[2] Wilkins, S. W., Stevenson, A. W., Nugent, K. A., Chapman, H., and Steenstrup, S., "On the concentration, focusing, and collimation of x-rays and neutrons using microchannel plates and configurations of holes," *Review of scientific instruments* **60**(6), 1026–1036 (1989).

[3] Chapman, H., Nugent, K., and Wilkins, S., "X-ray focusing using square channel-capillary arrays," *Review of scientific instruments* **62**(6), 1542–1561 (1991).

[4] Fraser, G. W., Lees, J. E., Pearson, J. F., Sims, M. R., and Roxburgh, K., "X-ray focusing using microchannel plates," in [*Multilayer and Grazing Incidence X-Ray/EUV Optics*], Hoover, R. B., ed., *Society of Photo-Optical Instrumentation Engineers (SPIE) Conference Series* **1546**, 41–52 (Jan. 1992).

[5] Kaaret, P., Geissbuhler, P., Chen, A., and Glavinas, E., "X-ray focusing using microchannel plates," *Appl. Opt.* **31**, 7339–7343 (Dec 1992).

[6] Gotz, D., Adami, C., Basa, S., Beckmann, V., Burwitz, V., Chipaux, R., Cordier, B., Evans, P., Godet, O., Goosmann, R., Meidinger, N., Meuris, A., Motch, C., Nandra, K., O'Brien, P., Osborne, J., Perinati, E., Rau, A., Willingale, R., Mercier, K., and Gonzalez, F., "The Microchannel X-ray Telescope on Board the SVOM Satellite," *ArXiv e-prints* (July 2015).

[7] Brunton, A., Martin, A., Fraser, G., and Feller, W., "A study of 8.5 μm microchannel plate x-ray optics," *Nuclear Instruments and Methods in Physics Research Section A: Accelerators, Spectrometers, Detectors and Associated Equipment* **431**(1), 356–365 (1999).